Morphologically controlled synthesis of colloidal upconversion nanophosphors and their shape-directed self-assembly

Xingchen Ye[a], Joshua E. Collins[b], Yijin Kang[a], Jun Chen[c], Daniel T. N. Chen[d], Arjun G. Yodh[d], and Christopher B. Murray[a,c,1]

[a]Department of Chemistry, University of Pennsylvania, Philadelphia, PA 19104; [b]Intelligent Material Solutions, Inc., Princeton, NJ 08540; [c]Department of Materials Science and Engineering, University of Pennsylvania, Philadelphia, PA 19104; and [d]Department of Physics and Astronomy, University of Pennsylvania, Philadelphia, PA 19104

Edited by Louis E. Brus, Columbia University, New York, NY, and approved October 25, 2010 (received for review June 27, 2010)

We report a one-pot chemical approach for the synthesis of highly monodisperse colloidal nanophosphors displaying bright upconversion luminescence under 980 nm excitation. This general method optimizes the synthesis with initial heating rates up to 100 °C/minute generating a rich family of nanoscale building blocks with distinct morphologies (spheres, rods, hexagonal prisms, and plates) and upconversion emission tunable through the choice of rare earth dopants. Furthermore, we employ an interfacial assembly strategy to organize these nanocrystals (NCs) into superlattices over multiple length scales facilitating the NC characterization and enabling systematic studies of shape-directed assembly. The global and local ordering of these superstructures is programmed by the precise engineering of individual NC's size and shape. This dramatically improved nanophosphor synthesis together with insights from shape-directed assembly will advance the investigation of an array of emerging biological and energy-related nanophosphor applications.

doped nanocrystals | superlattice | lanthanides | luminescence

Recent advances in synthesis and controlled assembly of monodisperse colloidal nanocrystals (NCs) into superlattice structures have enabled their applications in optics (1), electronics (2), magnetic storage (3), etc. Single- and multicomponent superlattices composed of spherical NCs are increasingly studied and a rich family of structures is now accessible (4, 5), where the electronic and magnetic interactions between the constituents gives rise to new cooperative properties (6, 7). New synthetic approaches are yielding nonspherical NCs with physical properties unobtainable by simply tuning the size of the spheres (8–11), providing an even broader array of nanoscale building blocks. The size and shape dependence of NC's biological activity (12, 13) and toxicity (14) is also of intense interest. However, the challenge of precisely controlling particle shape while maintaining uniformity in size and surface functionality has limited studies of NC environmental health and safety just as it has hindered efforts to organize anisotropic building blocks and to establish methods to capture their unique properties in NC superlattice thin films.

Lanthanide-doped nanophosphors are an emerging class of optical materials (15). These NCs often possess "peculiar" optical properties [e.g., quantum cutting (16) and photon upconversion (17)], allowing the management of photons that could benefit a variety of areas including biomedical imaging (18, 19) and therapy (20), photovoltaics (16, 21), solid state lighting (22), and display technologies (23). Colloidal upconversion nanophosphors (UCNPs) are capable of converting long-wavelength near-infrared excitation into short-wavelength visible emission through the long-lived, metastable excited states of the lanthanide dopants (24). In contrast to the Stokes-shifted emissions from semiconductor NCs or organic fluorophores and the multiphoton process employing fluorescent dyes, UCNPs offer several advantages including narrow emission bands tunable through the choice of dopants (25). With nonblinking emission and remarkable photostablity (18, 26), good brightness under low power continuous-wave laser excitation, low autofluorescence background and deep penetration lengths in biological systems, these materials are very attractive for bioimaging applications (18, 19). The hexagonal phase of $NaYF_4$ (β-$NaYF_4$) is one of the best host materials for upconversion due to its low phonon energies (27), being several orders of magnitude more efficient than the cubic, α-$NaYF_4$ phase (28). Several chemical approaches including coprecipitation (29) and hydrothermal synthesis (30) have been employed to synthesize β-$NaYF_4$-based UCNPs. However coprecipitation methods usually necessitate postsynthesis treatments to improve crystallinity of the products, and hydrothermal approaches typically involve long reaction times (ranging from a few hours up to several days) in pressurized reactors (e.g., autoclaves). Importantly, Yan et al. pioneered the synthesis of lanthanide fluoride NCs via the thermal decomposition of metal trifluoroacetate precursors (31, 32). Preparations of β-$NaYF_4$-based UCNPs through decomposition of mixed trifluoroacetates (33, 34) or through a two-step ripening process using the premade α-$NaYF_4$ NCs as precursors (35) have subsequently been reported. Despite these recent progresses, the crystal quality and monodispersity of the as-synthesized UCNPs using existing recipes are still far from ideal. In this contribution, we report a facile, one-pot method for the shape-controlled synthesis of highly monodisperse β-$NaYF_4$-based UCNPs. Furthermore, we demonstrate that the UCNPs with distinct morphologies (spheres, rods, hexagonal prisms, and plates) can be assembled into large-area superlattices (with individual domain up to ~200 μm^2) displaying simultaneous positional and orientational order. The symmetry/packing motifs of the superlattices are uniquely determined by the shape of individual NCs.

Results and Discussion

In this study all β-$NaYF_4$-based UCNPs are synthesized through thermal decompostion of sodium and lanthanide trifluoroacetates dissolved in a mixture of oleic acid and 1-octadecene. The use of molten salt bath as the heat reservoir ensures uniform heating of the solution that is rapid enough (up to 100 °C/minute) to overcome the disparity in decompostion temperature among various trifluoroacetate salts (*SI Appendix: Fig. S1*). Transmission electron microscopy (TEM) images of the UCNPs of various

Author contributions: X.Y., J.E.C., and C.B.M. designed research; X.Y., J.E.C., Y.K., J.C., and D.T.N.C. performed research; A.G.Y. contributed new reagents/analytic tools; X.Y. analyzed data; and X.Y. and C.B.M. wrote the paper.

The authors declare no conflict of interest.

This article is a PNAS Direct Submission.

[1]To whom correspondence should be addressed. E-mail: cbmurray@sas.upenn.edu.

This article contains supporting information online at www.pnas.org/lookup/suppl/doi:10.1073/pnas.1008958107/-/DCSupplemental.

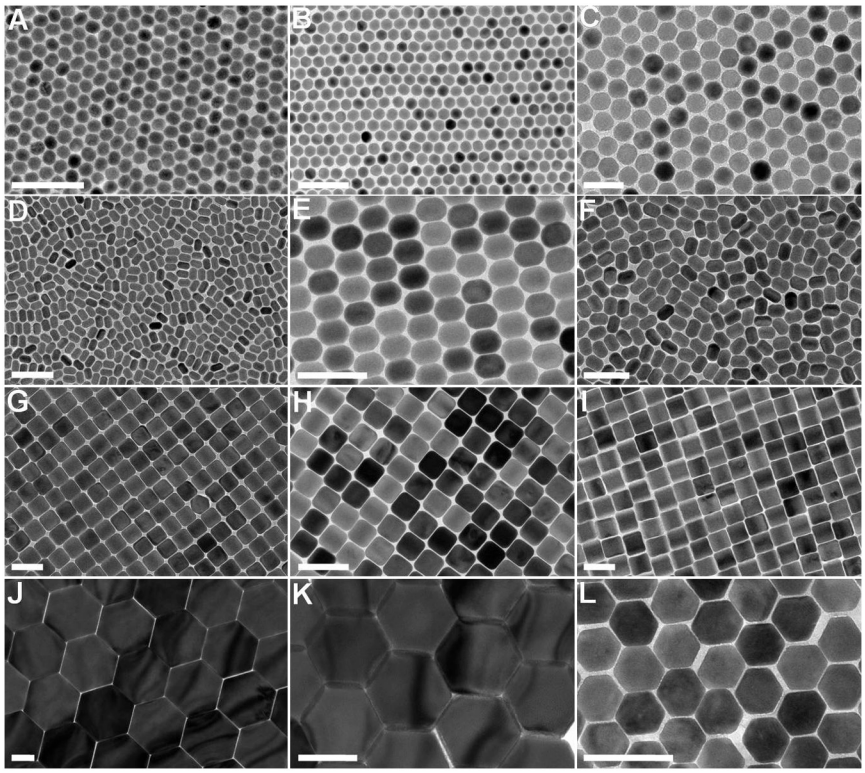

Fig. 1. TEM images of the β-$NaYF_4$-based UCNPs. (*A*, *D*, *G*, *J*) $NaYF_4$: Yb/Er (20/2 mol%) UCNPs. (*B*, *E*, *H*, *K*) $NaYF_4$: Yb/Tm (22/0.2 mol%) UCNPs. (*F*, *I*) $NaYF_4$: Yb/Ho (20/2 mol%) UCNPs. (C, L) $NaYF_4$: Yb/Ce/Ho (20/11/2 mol%) UCNPs. All scale bars represent 100 nm.

shapes and compositions are shown in Fig. 1. For the case of $NaYF_4$: Yb/Er (20/2 mol%)-an optimized composition for efficient upconversion (36), the morphologies of the UCNPs can be tuned from spherical NCs (Fig. 1*A*), to nanorods (NRs) (Fig. 1*D*), to hexagonal nanoprisms (Fig. 1*G*), and finally to hexagonal nanoplates (Fig. 1*J*) by adjusting the reaction time and/or the ratio of sodium to lanthanide trifluoroacetates. Powder X-ray diffraction (XRD) patterns confirm that all the $NaYF_4$: Yb/Er (20/2 mol%) UCNPs are of pure β-$NaYF_4$ phase (Fig. 2*A*). The XRD patterns of the spherical NCs and the NRs exhibit enhanced (h00) as well as diminished (002) reflections whereas a reversed trend is observed in the case of hexagonal nanoprisms and nanoplates. These results imply that the majority of spherical NCs and NRs are lying with a preference for the [0001] direction (*c*-axis) parallel to the glass substrates used for XRD while hexagonal nanoprisms and nanoplates are generally sitting with the c-axis perpendicular to the substrates (similar trends are confirmed separately by TEM). High-resolution TEM (HRTEM) image of a single spherical NC shows clear lattice fringes associated with the $(10\,\bar{1}0)$, $(10\,\bar{1}1)$, and (0001) crystal planes, respectively (Fig. 2*B*). Lattice fringes corresponding to the (0001) planes appear along the NRs, indicating that the NRs grow along the *c*-axis (Fig. 2*C* and *SI Appendix: Fig. S2A*). HRTEM analysis also reveals that the "cube-like" projections are coming from hexagonal prisms composed of six square or rectangular $\{10\,\bar{1}0\}$ side facets with two hexagonal bases belonging to the {0001} planes (Fig. 2*D* and *SI Appendix: Fig. S2B*). The formation of NRs and hexagonal nanoprisms is determined by a delicate interplay between the growth rates of {0001} and $\{10\,\bar{1}0\}$ planes at different growth stages. This observation contrasts with previous studies where shape evolution of the β-$NaYF_4$ NCs was dominated by controlling the Ostwald-ripening process (35). Furthermore, dynamic light scattering experiments that probe the hydrodynamic size of the dispersed NRs and hexagonal nanoprisms show results consistent with the largest dimensions of individual NCs measured from the TEM images (*SI Appendix: Fig. S4*). In addition, quantitative elemental analyses based on inductively coupled plasma optical emission spectrometry (ICP-OES) indicate the proportional incorporation of precursor lanthanide elements into the final UCNPs (*SI Appendix: Table S2*). By increasing the sodium to lanthanide ratio and the reaction time, hexagonal nanoplates with an edge length of 133 5 nm and a thickness of 104 8 nm are obtained (Fig. 1*J* and *SI Appendix: Fig. S5*). HRTEM image taken from the edge region confirms its high crystallinity (Fig. 2*E*). Although the present results do not rule out the possibility of cubic to hexagonal ($\alpha \rightarrow \beta$) phase transition very early during the growth, no definitive signature of α phase is observed and the high reaction temperature (~330 °C) favors the formation of β-$NaYF_4$ UCNPs.

The $NaYF_4$: Yb/Er (20/2 mol%) UCNPs exhibit intense upconversion luminescence under 980 nm excitation (Fig. 2*F* and *SI Appendix: Fig. S6*). Three visible emission bands centered at 525, 542, and 655 nm are observed, attributable to the radiative transitions from the ($^2H_{11/2}$, $^4S_{3/2}$) (green) and from the $^4F_{9/2}$ (red) excited states to the $^4I_{15/2}$ ground state of Er^{3+}, respectively. The activator Yb^{3+}, capable of absorbing the 980 nm near-infrared light efficiently, transfers its energy sequentially to nearby Er^{3+} through the $^2F_{5/2}(Yb^{3+}) \rightarrow {}^4I_{11/2}(Er^{3+})$ process, pumping the Er^{3+} to its emitting levels. The multiphonon relaxation processes help bridge the different excited states of Er^{3+}, giving rise to distinct emission peaks (*SI Appendix: Fig. S8*). The $NaYF_4$: Yb/Er (20/2 mol%) UCNPs obtained display size-dependent optical properties (Fig. 2*F* and *SI Appendix: Fig. S9*): Both the total intensity of emission and the intensity ratio of green to red emission increase as NCs get larger. These relationships can be ascribed to the fact that as the size of the NCs decreases, surface defects- and ligands-induced quenching of upconversion become more important, which modifies the relative population among various excited states through phonon-assisted nonradiative relaxations (36). Therefore, engineering not only the dopant con-

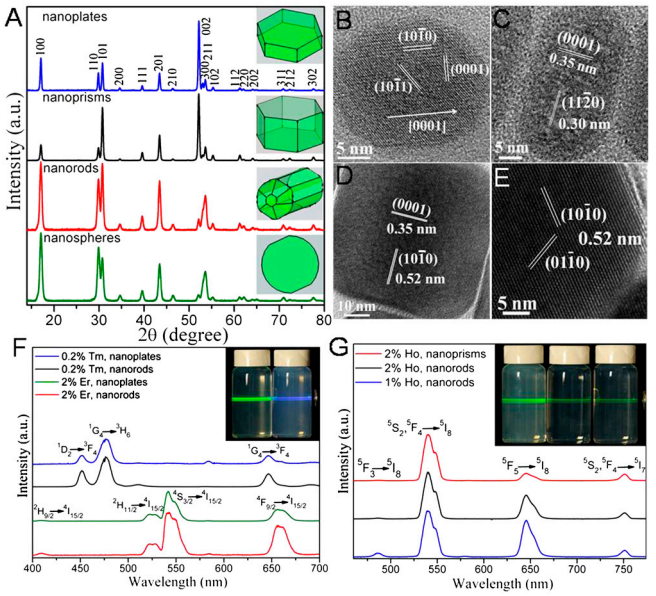

Fig. 2. Structural and optical characterization of the β-$NaYF_4$-based UCNPs. (*A*) Powder XRD patterns of the $NaYF_4$: Yb/Er (20/2 mol%) UCNPs with different shapes. The peaks are indexed according to the standard XRD pattern of β-$NaYF_4$ (JCPDS file number: 28-1192). Insets are the corresponding geometrical models. (*B*) HRTEM image of a spherical $NaYF_4$: Yb/Er (20/2 mol%) UCNP. (*C*) HRTEM image of a $NaYF_4$: Yb/Er (20/2 mol%) NR. (*D*) HRTEM image of a $NaYF_4$: Yb/Er (20/2 mol%) hexagonal nanoprism. (*E*) HRTEM image taken from the edge of a $NaYF_4$: Yb/Er (20/2 mol%) hexagonal nanoplate. (*F*) Room temperature upconversion emission spectra of the $NaYF_4$: Yb/Er (20/2 mol%) and $NaYF_4$: Yb/Tm (22/0.2 mol%) UCNPs dispersed in hexane. Inset: Photographs of the upconversion luminescence from the $NaYF_4$: Yb/Er (20/2 mol%) (left) and $NaYF_4$: Yb/Tm (22/0.2 mol%) (right) NR dispsersions under 980 nm diode laser excitation. (*G*) Room temperature upconversion emission spectra of the $NaYF_4$: Yb/Ho (20/2 mol%) and $NaYF_4$: Yb/Ho (20/1 mol%) UCNPs dispersed in hexane. Inset: Photographs of the upconversion luminescence from the $NaYF_4$: Yb/Ho (20/2 mol%) nanoprism (left), $NaYF_4$: Yb/Ho (20/2 mol%) NR (center) and $NaYF_4$: Yb/Ho (20/1 mol%) NR (right) dispersions under 980 nm diode laser excitation.

centration but also the surface functionalities of the UCNPs can be an effective means of tuning the upconversion luminescence.

To demonstrate the generality of the synthesis method and further tailor the upconversion emissions, we try several other dopant combinations including Yb/Tm, Yb/Ho, and Yb/Ho/Ce for the β-$NaYF_4$-based UCNPs. TEM images of the $NaYF_4$: Yb/Tm (22/0.2 mol%) UCNPs with different morphologies are shown in Fig. 1*B* (spherical NCs), Fig. 1*E* (NRs), Fig. 1*H* (hexagonal nanoprisms), and Fig. 1*K* (hexagonal nanoplates), respectively. Upon 980 nm excitation, these hexagonal phase UCNPs (*SI Appendix: Fig. S12*) emit bright blue upconversion luminescence arising from the trivalent thulium $^1D_2 \rightarrow {}^3F_4$ and $^1G_4 \rightarrow {}^3H_6$ transitions (Fig. 2*F*). In addition, predominantly green upconversion emissions are observed from the hexagonal phase (*SI Appendix: Fig. S14*) $NaYF_4$: Yb/Ho (20/2 mol%) NRs and nanoprisms UCNPs (Figs. 1 *F* and *I* and 2*G*). The intensity ratio of green to red emission from the NRs increases as the Ho^{3+} concentration increases from 1% to 2%, owing to the enhanced energy transfer from the Yb^{3+} sensitizers to adjacent Ho^{3+} ions (37). Furthermore, trivalent Ce^{3+} ions are introduced to modulate the upconversion profiles of the $NaYF_4$: Yb/Ho (20/2 mol%) UCNPs. The parity-allowed $4f \rightarrow 5d$ transition in the Ce^{3+} ions can effectively depopulate the green-emitting $^5F_4/^5S_2$ states of Ho^{3+} while increasing the population of the red-emitting $^5F_5$ state of Ho^{3+} through two cross-relaxation pathways (*SI Appendix: Fig. S8*): $^5F_4/^5S_2(Ho^{3+}) + {}^2F_{5/2}(Ce^{3+}) \rightarrow {}^5F_5(Ho^{3+}) + {}^2F_{7/2}(Ce^{3+})$ and $^5I_6(Ho^{3+}) + {}^2F_{5/2}(Ce^{3+}) \rightarrow {}^5I_7(Ho^{3+}) + {}^2F_{7/2}(Ce^{3+})$ (38). The as-synthesized $NaYF_4$: Yb/Ce/Ho (20/11/2 mol%) spherical NCs (Fig. 1*C*) and hexagonal nanoplates (Fig. 1*L*) display predominantly red emission under 980 nm excitation although the total intensity of emission is much weaker than other UCNPs (*SI Appendix: Fig. S15*). Powder XRD patterns confirm that both samples are of pure hexagonal phase (*SI Appendix: Figs. S16 and S17*). The systematic peak shifts to lower angles compared to the standard XRD pattern of β-$NaYF_4$ imply the partial substitution of Y^{3+} ions by larger Ce^{3+} ions in the β-$NaYF_4$ lattice (Y^{3+}, $r = 1.159$ Å; Ce^{3+}, $r = 1.283$ Å) (39), which results in the expansion of the unit cell. This Ce^{3+} doping differs from previous reports where lanthanide elements with large ionic radii (e.g., $La^{3+} = 1.300$ Å) could not be incorporated into the β-$NaYF_4$ lattice (23). In addition, uniform undoped β-$NaYF_4$ NRs can also be synthesized by the present method (*SI Appendix: Fig. S19*).

Superlattices composed of anisotropic NCs have attracted great interest due to the rich phase behaviors and the potential for emergent collective properties (40). Here we explore the intriguing structural diversity of ordered nanocrystal assemblies using β-$NaYF_4$ NRs and the β-$NaYF_4$-based UCNPs. We employ an interfacial assembly strategy that can produce continuous and uniform nanocrystal superlattice films (41). When 15 μL of hexane solution of the β-$NaYF_4$ NRs with an aspect ratio (AR) of ~1.4 is drop-cast onto the viscous and weakly polar ethylene glycol (EG) surface and the solvent is allowed to slowly evaporate, large-area NR superlattices comprised of monolayer and double-layer domains are obtained depending on the concentration of NRs in the dispersion (Fig. 3 *A* and *B*). The NRs preferentially align with their c-axis parallel to the substrate, exhibiting both positional and orientation order on the scale of tens of micrometers, as confirmed by the sharp small-angle electron diffraction patterns (SAED). The striking in-plane ordering of the NR superlattices is also revealed by the selected-area wide-angle electron diffraction patterns (SAWED), whose spots are due to diffraction of crystallographic lattice planes. Specifically, the strong (002) diffraction spots are arising from the anisotropic rod-shape of the individual NCs and their mutual alignment along the c-axis. Interestingly, the appearance of (h00) and simultaneous absence of (110) diffraction spots, together with the recognition that the β-$NaYF_4$ NRs are enclosed by the $\{10\,\bar{1}0\}$ facets, allow us to conclude that the NRs are azimuthally aligned along their $\{10\,\bar{1}0\}$ crystal facets (*SI Appendix: Fig. S22*). The superlattice formation is accounted for by the in-plane, dense packing of the β-$NaYF_4$ NRs, possessing a hexagonal cross section and also the interaction of ligands, contributing to the attractions between adjacent NRs. Further evidence that supports the explanation is the lateral displacement between neighboring layers in the β-$NaYF_4$ NR superlattices (*SI Appendix: Fig. S23*). Liquid crystalline order has been observed in concentrated NR dispersions (42) and NR films prepared by controlled evaporation (43, 44) or by Langmuir-Blodgett assembly (45). Here we have also employed polarizing optical microscope to study the ordering of NR films. Optical micrographs (Fig. 3*C* and *SI Appendix: Fig. S25*) indicate domains that are strongly birefringent due to the alignment of NRs. The multidomain nature of the NR films is also confirmed by the atomic force microscopy (AFM). We anticipate that NRs with larger AR (>3) would be better suited for the formation of liquid crystalline phases using the present assembly methodology. β-$NaYF_4$ NRs with an AR of ~2.0 have also been used to study the shape-directed assembly behavior: monolayer and double-layer superlattices are obtained by depositing 15 μL of NR dispersion (Fig. 4 *A* and *B*). However, when 40 μL of NR dispersion is used, the NRs tend to orient vertically in the film with well crystallized domains up to ~200 μm^2 (Fig. 4*C*), as seen from the corresponding SAWED pattern. Each domain is composed of hexagonally closed-packed perpendicularly aligned NRs

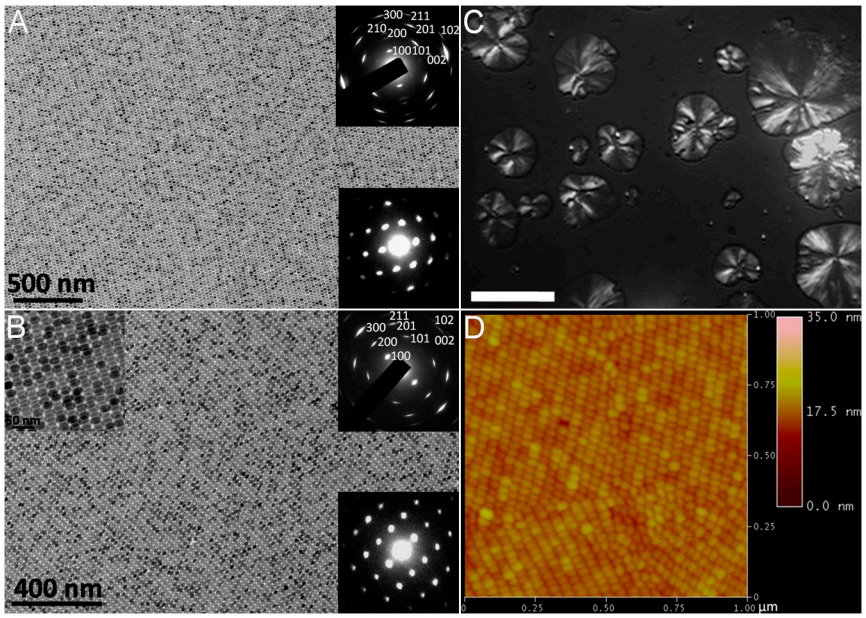

Fig. 3. $NaYF_4$ (AR = 1.4) NR superlattices. (*A*) TEM image of a monolayer superlattice of NRs that are oriented parallel to the substrate. The upper right inset is the corresponding SAWED pattern and the lower right inset is the corresponding SAED pattern. Both patterns are acquired from an area of ~6.5 μm^2. (*B*) TEM image of a double-layer superlattice of NRs that are oriented parallel to the substrate. The upper left inset is the high-magnification TEM image acquired from the same domain. The upper right inset is the corresponding SAWED pattern and the lower right inset is the corresponding SAED pattern. Both patterns are acquired from an area of ~6.5 μm^2. (*C*) Optical micrographs of the $NaYF_4$ (AR = 1.4) NR superlattices observed with crossed polarizers. The scale bar represents 30 μm. (*D*) AFM image showing the domain boundaries of the NR superlattices.

(Fig. 4*D*). This general method to vertically align and assemble NRs maybe of interest for various applications such as photovoltaics (46), plasmonic biosensing (47), and magnetic information storage (3).

The ordering of the as-deposited hexagonal nanoprisms and nanoplates superlattices is also strongly dependent on the detailed geometry of individual NCs: In the hexagonal nanoprism assemblies (Fig. 5*A* and *SI Appendix: Fig. S27*), each "cube-like" nanoprism has six neighbors. However, the packing symmetry deviates from the square lattice expected for perfect cubes. The arrangement, in light of recent theoretical work on the packing of fourfold rotationally symmetric superdisks, can be described as the Λ_1-lattice packing (48). Due to the reduced shape symmetry, the hexagonal nanoprisms self-organize into a configuration that maximizes the packing density. On the other hand, hexagonal nanoplates self assemble into close-packed hexagonally ordered

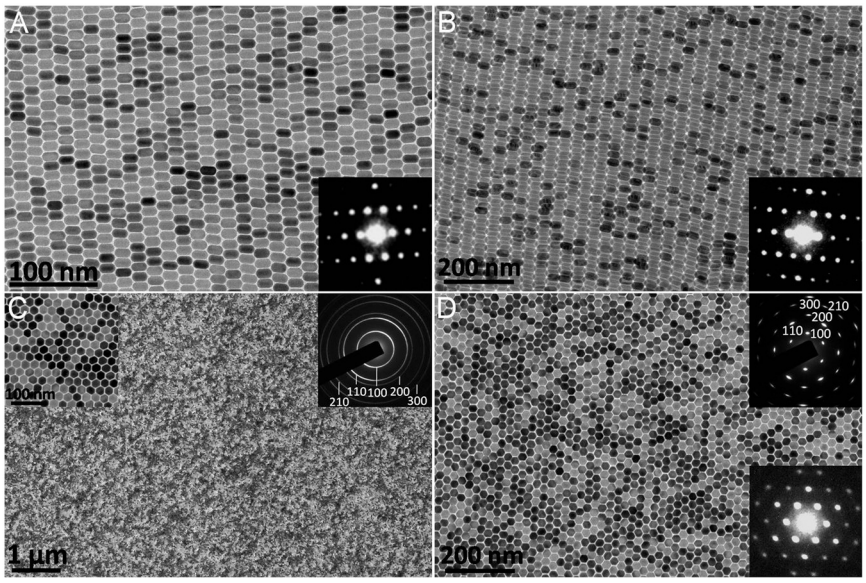

Fig. 4. $NaYF_4$ (AR = 2.0) NR superlattices. (*A*) TEM image of a monolayer superlattice of NRs that are oriented parallel to the substrate. The lower right inset is the corresponding SAED pattern acquired from an area of ~2 μm^2. (*B*) TEM image of a double-layer superlattice of NRs that are oriented parallel to the substrate. The lower right inset is the corresponding SAED pattern acquired from an area of ~2 μm^2. (*C*) TEM image of a monolayer of vertically aligned NR superlattices. The upper left inset is the high-magnification TEM image showing the hexagonally closed-packed array of NRs. The upper right inset is the corresponding SAWED pattern acquired from an area of ~60 μm^2. (*D*) TEM image of a closed-packed hexagonally ordered array of vertically aligned NRs. The upper right inset is the corresponding SAWED pattern and the lower right inset is the corresponding SAED pattern. Both patterns are acquired from an area of ~6.5 μm.

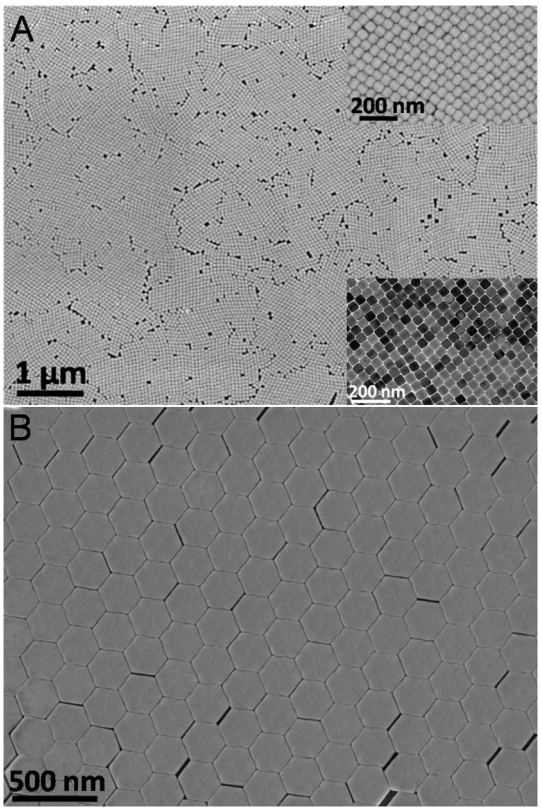

Fig. 5. Hexagonal nanoprism and nanoplate superlattices. (*A*) SEM image of a monolayer superlattice of $NaYF_4$: Yb/Tm (22/0.2 mol%) hexagonal nanoprisms. The upper right and lower right insets are the high-magnification SEM and TEM images, respectively. (*B*) SEM image of the self-assembled superlattice of $NaYF_4$: Yb/Er (20/2 mol%) hexagonal nanoplates.

arrays (Fig. 5*B* and *SI Appendix: Fig. S28–30*), consistent with the sixfold symmetry of nanoplates.

Conclusions

In summary, we have shown that under different synthetic conditions, $NaYF_4$-based UCNPs develop regular facets and finally evolve into a diverse family of morphologies (spheres, rods, hexagonal prisms, and plates) in accordance with the underlying hexagonal unit-cell symmetry. Monodisperse UCNPs with distinct shapes are model systems to advance the understanding of the shape-directed assembly/packing behaviors of nanocolloids, but also open new opportunities in fields such as bioimaging (18, 19) and photodynamic therapy (20, 49). Programming anisotropic NCs to assemble into desired two- and three-dimensional patterns enables the production of complex nanoscale architectures useful for applications such as solar cells (46) and plasmonic metamaterials (50).

Materials and Methods

Synthesis of Upconversion Nanophosphors (UCNPs). All syntheses were carried out using standard Schlenk techniques. 1-Octadecene (ODE; technical grade, 90%), oleic acid (OA; technical grade, 90%), $Na(CF_3COO)$ and EG were purchased from Sigma Aldrich. $RE(CF_3COO)_3$ (RE = Y, Yb, Er, Tm) and Y, Yb, and Er 1,000 ppm ICP standard solutions were purchased from GFS Chemicals, Inc. $Ho(CF_3COO)_3$ was purchased from Rare Earth Products, Inc. $Ce(CF_3COO)_3$ was prepared according to the literature method (51) using cerium(III) carbonate hydrate (Aldrich) and trifluoroacetic acid (Alfa Aesar) as the precursors. A typical protocol for the synthesis of hexagonal phase $NaYF_4$-based UCNPs is described below: certain amount of $Na(CF_3COO)$ and $RE(CF_3COO)_3$ (see *SI Appendix: Table S1* for details) together with 15 mL of ODE and 15 mL of OA were added to a three-necked flask. The mixture was then heated under vacuum at 100 °C for 45 min to form a transparent, yellow solution. The reaction flask was flushed with N_2 for 5 min and was then placed into a molten $NaNO_3/KNO_3$ (1:1 mass ratio) salt bath that was stabilized for 342 °C. A large amount of white smoke was produced after about 1.5 min, indicating the decomposition of metal trifluoroacetates (51). After 20–35 min of reaction under N_2 flow and vigorous magnetic stirring, the solution was cooled down by adding 15 mL of ODE. The products were isolated by adding ethanol and centrifugation. Due to the mondispersity of the as-synthesized samples, no size-selective fractionation is needed. The UCNPs were redispersed in hexane with nanocrystal concentration of about 5.0 mg/mL.

Assembly of UCNPs into Superlattices. The assembly was done using a variant of the interfacial assembly method recently developed by our group (41). Briefly, a $1.5 \times 1.5 \times 1$ cm^3 Teflon well was half-filled with EG. Certain amount of UCNP dispersions (see main text for details) was drop-cast onto the EG surface and the well was then covered by a glass slide to slow down solvent evaporation. After 40 min, the nanocrystal film was transferred onto glass substrates or TEM grids (300-mesh) that was further dried under vacuum to remove extra EG.

Structural and Optical Characterization. TEM images and electron diffraction patterns were taken on a JEM-1400 microscope operating at 120 kV. HRTEM images were taken on a JEOL 2010F microscope operating at 200 kV. Scanning electron microscopy (SEM) was performed on a JEOL 7500F HRSEM. Power XRD patterns were obtained on the Rigaku Smartlab diffractometer at a scanning rate of 0.1° min^{-1} in the 2θ range from 10° to 80° (Cu Kα radiation, $\lambda = 1.5418$ Å). For XRD measurement, samples were prepared by depositing hexane solutions of nanocrystals onto a glass substrate. Dynamic light scattering (DLS) measurements were performed on a Delsa Nano C system (Beckman Coulter). AFM height images were obtained on the DI Multimode AFM. Quantitative elemental analysis was carried out with ICP-OES on a SPECTRO GENESIS ICP spectrometer. Room temperature upconversion emission spectra were acquired with the fiber-optically coupled USB4000 fluorescence spectrometer (Ocean Optics) using an external continuous-wave laser centered at ~980 nm as the excitation source (Dragon Lasers). The optical photographs of the emitting UCNPs were taken using a Nikon D300 digital camera. Nanorod superlattices on glass substrates were imaged under crossed polarizers using a Leica DMRX upright microscope equipped with a charge-coupled device (CCD) camera (Hitachi KP-M1U).

ACKNOWLEDGMENTS. We thank Douglas M. Yates and Lolita Rotkina at the Penn Regional Nanotechnology Facility for support in electron microscopy. X.Y. acknowledges primary support from the Department of Energy Basic Energy Science division through award DE-SC0002158 while C.B.M. received partial support for his supervisor role from the Department of Energy Basic Energy Science division through award DE-SC0002158 with secondary support from the National Science Foundation (NSF) Solar initiative through award DMS-0935165. Y.K.'s work on elemental analysis was supported by the Army Research Office (ARO) through MURI W911NF-08-1-0364 and J.C.'s work on structural characterization and analysis was partially supported by the NSF-funded Materials Research Science and Engineering Centers (MRSEC) at the University of Pennsylvania (DMR-0520020). J.E.C. acknowledges the supports from the Nanotechnology Institute of the Commonwealth of Pennsylvania's Ben Franklin Technology Development Authority and the National Institute of Biomedical Imaging and Bioengineering through the National Institute of Health (NIH) Small Business Technology Transfer (STTR) Phase I grant (Award number: R41EB008959). D.T.N.C. and A.G.Y. acknowledge the financial supports from NSF (DMR-0505048 and MRSEC DMR-0520020) and NASA (NNX08AO0G).

1. Tao A, Sinsermsuksakul P, Yang P (2007) Tunable plasmonic lattices of silver nanocrystals. *Nature Nanotechnol* 2:435–440.
2. Talapin DV, Murray CB (2005) PbSe nanocrystal solids for *n*- and *p*-channel thin film field-effect transistors. *Science* 310:86–89.
3. Sun SH, Murray CB, Weller D, Folks L, Moser A (2000) Monodisperse FePt nanoparticles and ferromagnetic FePt nanocrystal superlattices. *Science* 287:1989–1992.
4. Shevchenko EV, Talapin DV, Kotov NA, O'Brien S, Murray CB (2006) Structural diversity in binary nanoparticle superlattices. *Nature* 439:55–59.
5. Talapin DV, et al. (2009) Quasicrystalline order in self-assembled binary nanoparticle superlattices. *Nature* 461:964–967.
6. Urban JJ, Talapin DV, Shevchenko EV, Kagan CR, Murray CB (2007) Synergism in binary nanocrystal superlattices leads to enhanced p-type conductivity in self-assembled $PbTe/Ag_2Te$ thin films. *Nature Mater* 6:115–121.
7. Cheon J, et al. (2006) Magnetic superlattices and their nanoscale phase transition effects. *Proc Natl Acad Sci USA* 103:3023–3027.
8. Peng XG, et al. (2000) Shape control of CdSe nanocrystals. *Nature* 404:59–61.
9. Jana NR, Gearheart L, Murphy CJ (2001) Wet chemical synthesis of high aspect ratio cylindrical gold nanorods. *J Phys Chem B* 105:4065–4067.
10. Sun YG, Xia YN (2002) Shape-controlled synthesis of gold and silver nanoparticles. *Science* 298:2176–2179.

11. Jin RC, et al. (2003) Controlling anisotropic nanoparticle growth through plasmon excitation. *Nature* 425:487–490.
12. Chithrani BD, Ghazani AA, Chan WCW (2006) Determining the size and shape dependence of gold nanoparticle uptake into mammalian cells. *Nano Lett* 6:662–668.
13. Gratton SEA, et al. (2008) The effect of particle design on cellular internalization pathways. *Proc Natl Acad Sci USA* 105:11613–11618.
14. Auffan M, et al. (2009) Towards a definition of inorganic nanoparticles from an environmental, health and safety perspective. *Nature Nanotechnol* 4:634–641.
15. Wang F, Liu XG (2009) Recent advances in the chemistry of lanthanide-doped upconversion nanocrystals. *Chem Soc Rev* 38:976–989.
16. van der Ende BM, Aarts L, Meijerink A (2009) Near-infrared quantum cutting for photovoltaics. *Adv Mater* 21:3073–3077.
17. Auzel F (2004) Upconversion and anti-stokes processes with f and d ions in solids. *Chem Rev* 104:139–173.
18. Wu SW, et al. (2009) Non-blinking and photostable upconverted luminescence from single lanthanide-doped nanocrystals. *Proc Natl Acad Sci USA* 106:10917–10921.
19. Kobayashi H, et al. (2009) In vivo multiple color lymphatic imaging using upconverting nanocrystals. *J Mater Chem* 19:6481–6484.
20. Zhang P, Steelant W, Kumar M, Scholfield M (2007) Versatile photosensitizers for photodynamic therapy at infrared excitation. *J Am Chem Soc* 129:4526–4527.
21. Shalav A, Richards BS, Trupke T, Kramer KW, Gudel HU (2005) Application of $NaYF_4$: Er^{3+} up-converting phosphors for enhanced near-infrared silicon solar cell response. *Appl Phys Lett* 86:013505.
22. Sivakumar S, van Veggel FCJM, Raudsepp M (2005) Bright white light through up-conversion of a single NIR source from sol-gel-derived thin film made with Ln^{3+}-doped LaF_3 nanoparticles. *J Am Chem Soc* 127:12464–12465.
23. Wang F, et al. (2010) Simultaneous phase and size control of upconversion nanocrystals through lanthanide doping. *Nature* 463:1061–1065.
24. Heer S, Kompe K, Gudel HU, Haase M (2004) Highly efficient multicolour upconversion emission in transparent colloids of lanthanide-doped $NaYF_4$ nanocrystals. *Adv Mater* 16:2102–2105.
25. Wang F, Liu XG (2008) Upconversion multicolor fine-tuning: Visible to near-infrared emission from lanthanide-doped $NaYF_4$ nanoparticles. *J Am Chem Soc* 130:5642–5643.
26. Park YI, et al. (2009) Nonblinking and nonbleaching upconverting nanoparticles as an optical imaging nanoprobe and T_1 magnetic resonance imaging contrast agent. *Adv Mater* 21:4467–4471.
27. Suyver JF, et al. (2006) Upconversion spectroscopy and properties of $NaYF_4$ doped with Er^{3+}, Tm^{3+} and/or Yb^{3+}. *J Lumin* 117:1–12.
28. Kramer KW, et al. (2004) Hexagonal sodium yttrium fluoride based green and blue emitting upconversion phosphors. *Chem Mater* 16:1244–1251.
29. Yi GS, et al. (2004) Synthesis, characterization, and biological application of size-controlled nanocrystalline $NaYF_4$: Yb, Er infrared-to-visible up-conversion phosphors. *Nano Lett* 4:2191–2196.
30. Zeng JH, Su J, Li ZH, Yan RX, Li YD (2005) Synthesis and upconversion luminescence of hexagonal-phase $NaYF_4$: Yb, Er^{3+} phosphors of controlled size and morphology. *Adv Mater* 17:2119–2123.
31. Zhang YW, Sun X, Si R, You LP, Yan CH (2005) Single-crystalline and monodisperse LaF_3 triangular nanoplates from a single-source precursor. *J Am Chem Soc* 127:3260–3261.
32. Mai HX, et al. (2006) High-quality sodium rare-earth fluoride nanocrystals: Controlled synthesis and optical properties. *J Am Chem Soc* 128:6426–6436.
33. Yi GS, Chow GM (2006) Synthesis of hexagonal-phase $NaYF_4$: Yb, Er and $NaYF_4$: Yb, Tm nanocrystals with efficient up-conversion fluorescence. *Adv Funct Mater* 16:2324–2329.
34. Chan EM, et al. (2010) Reproducible, high-throughput synthesis of colloidal nanocrystals for optimization in multidimensional parameter space. *Nano Lett* 10:1874–1885.
35. Mai HX, Zhang YW, Sun LD, Yan CH (2007) Size- and phase-controlled synthesis of monodisperse $NaYF_4$: Yb, Er nanocrystals from a unique delayed nucleation pathway monitored with upconversion spectroscopy. *J Phys Chem C* 111:13730–13739.
36. Mai HX, Zhang YW, Sun LD, Yan CH (2007) Highly efficient multicolor up-conversion emissions and their mechanisms of monodisperse $NaYF_4$: Yb, Er core and core/shell-structured nanocrystals. *J Phys Chem C* 111:13721–13729.
37. Naccache R, Vetrone F, Mahalingam V, Cuccia LA, Capobianco JA (2009) Controlled synthesis and water dispersibility of hexagonal phase $NaGdF_4$: Ho^{3+}/Yb^{3+} nanoparticles. *Chem Mater* 21:717–723.
38. Chen GY, Liu HC, Somesfalean G, Liang HJ, Zhang ZG (2009) Upconversion emission tuning from green to red in Yb^{3+}/Ho^{3+}-codoped $NaYF_4$ nanocrystals by tridoping with Ce^{3+} ions. *Nanotechnology* 20:385704.
39. Shannon RD (1976) Revised effective ionic radii and systematic studies of interatomic distances in halides and chalcogenides. *Acta Crystallogr A* 32:751–767.
40. Glotzer SC, Solomon MJ (2007) Anisotropy of building blocks and their assembly into complex structures. *Nature Mater* 6:557–562.
41. Dong A, Chen J, Vora PM, Kikkawa JM, Murray CB (2010) Binary nanocrystal superlattice membranes self-assembled at the liquid-air interface. *Nature* 466:474–477.
42. Li LS, Walda J, Manna L, Alivisatos AP (2002) Semiconductor nanorod liquid crystals. *Nano Lett* 2:557–560.
43. Talapin DV, et al. (2004) CdSe and CdSe/CdS nanorod solids. *J Am Chem Soc* 126:12984–12988.
44. Ming T, et al. (2008) Ordered gold nanostructure assemblies formed by droplet evaporation. *Angewandte Chemie International Edition* 47:9685–9690.
45. Kim F, Kwan S, Akana J, Yang PD (2001) Langmuir-Blodgett nanorod assembly. *J Am Chem Soc* 123:4360–4361.
46. Huynh WU, Dittmer JJ, Alivisatos AP (2002) Hybrid nanorod-polymer solar cells. *Science* 295:2425–2427.
47. Kabashin AV, et al. (2009) Plasmonic nanorod metamaterials for biosensing. *Nature Mater* 8:867–871.
48. Jiao Y, Stillinger FH, Torquato S (2008) Optimal packings of superdisks and the role of symmetry. *Phys Rev Lett* 100:245504.
49. Ungun B, et al. (2009) Nanofabricated upconversion nanoparticles for photodynamic therapy. *Opt Express* 17:80–86.
50. Stebe KJ, Lewandowski E, Ghosh M (2009) Oriented assembly of metamaterials. *Science* 325:159–160.
51. Roberts JE (1961) Lanthanum and neodymium salts of trifluoroacetic acid. *J Am Chem Soc* 83:1087–1088.